

Continuum-based rock model of a reservoir dolostone with four orders of magnitude in pore sizes

Sven Roth, Bibhu Biswal, Ghazaleh Afshar, Rudolf J. Held, Pål-Eric Øren, Lars Inge Berge, and Rudolf Hilfer

ABSTRACT

A continuum-based pore-scale representation of a dolomite reservoir rock is presented, containing several orders of magnitude in pore sizes within a single rock model. The macroscale rock fabric from a low-resolution x-ray microtomogram was combined with microscale information gathered from high-resolution two-dimensional electron microscope images. The low-resolution x-ray microtomogram was segmented into six separate rock phases in terms of mineralogy, matrix appearances, and open- versus crystal-filled molds. These large-scale rock phases were decorated (modeled) with geometric objects, such as different dolomite crystal types and anhydrite, according to the high-resolution information gathered from the electron microscope images. This procedure resulted in an approximate three-dimensional representation of the diagenetically transformed rock sample with respect to dolomite crystal sizes, porosity, appearance, and volume of different matrix phases and pore/matrix/cement ratio.

The resulting rock model contains a pore-size distribution ranging from moldic macropores (several hundred micrometers in diameter) down to mudstone micropores ($<1 \mu\text{m}$ in diameter). This allows us to study the effect and contribution of different pore classes to the petrophysical properties of the rock. Higher resolution x-ray tomographs of the same rock were used as control volumes for the pore-size distribution of

AUTHORS

SVEN ROTH ~ *Numerical Rocks AS, 7041 Trondheim, Norway; sven@numericalrocks.com*

Sven Roth received his M.Sc. degree in geology (1999) and his Ph.D. in carbonate sedimentology (2003) from the Christian-Albrechts University of Kiel, Germany. After postdoctorates at the Leibniz Institute of Marine Sciences and at the Leibniz-Laboratory for Radiometric Dating and Isotope Research in Kiel and at the Université de Provence in Marseille, he joined Numerical Rocks in 2006 and currently is a technology development manager in geology.

BIBHU BISWAL ~ *Institut für Computerphysik, Universität Stuttgart, Pfaffenwaldring 27, 70569 Stuttgart, Germany; present address: S.V. College, University of Delhi, New Delhi 110 021, India*

Bibhu Biswal obtained his Ph.D. (physical sciences) in 1994 from Jawaharlal Nehru University, Delhi. He is now an associate professor in physics at S. V. College, University of Delhi, India. His main research contributions are in the study of phase transitions in disordered magnets, computational reconstruction of rock microstructure, and their characterization, analysis, and prediction of physical parameters from digital images.

GHAZALEH AFSHAR ~ *Institut für Computerphysik, Universität Stuttgart, Pfaffenwaldring 27, 70569 Stuttgart, Germany; ghazaleh.afshar@gmail.com*

Ghazaleh Afshar received her B.Sc. degree in physics from the Sharif University of Technology in Tehran, Iran, in 2007 and her M.Sc. degree in physics from the University of Stuttgart, Germany, in 2009. Currently, she is a Ph.D. student at the Max Planck Institute for Dynamics and Self-Organization in Göttingen, Germany.

RUDOLF J. HELD ~ *Statoil ASA, 7005 Trondheim, Norway; rujh@statoil.com*

Rudolf Held holds an M.Sc. degree in geology from the Technical University Clausthal, Germany, and a Ph.D. in environmental engineering from Princeton University, New Jersey. He has worked in gold exploration and environmental and reservoir engineering and currently is a principal researcher at the Statoil Research Center in Trondheim, Norway.

Copyright ©2011. The American Association of Petroleum Geologists. All rights reserved.

Manuscript received May 28, 2010; provisional acceptance July 28, 2010; revised manuscript received October 29, 2010; final acceptance December 3, 2010.

DOI:10.1306/12031010092

PÅL-ERIC ØREN ~ *Numerical Rocks AS, 7041 Trondheim, Norway; peoe@numericalrocks.com*

Pål-Eric Øren holds an M.Sc. degree in chemical engineering from the University of Michigan and a Ph.D. in petroleum engineering from the University of New South Wales, Australia. He is the technical director and cofounder of Numerical Rocks AS.

LARS INGE BERGE ~ *Statoil ASA, 7005 Trondheim, Norway; liber@statoil.com*

Lars Inge Berge holds an M.Sc. degree in physics from the Norwegian Institute of Technology, Trondheim, and a Ph.D. in physics from the University of Oslo, Norway. He has worked in condensed matter physics, hydrates, and multiphase flow in pipes. Currently, he is a manager at the Statoil Research Center, Trondheim, Norway, and works in the field of reservoir engineering.

RUDOLF HILFER ~ *Institut für Computerphysik, Universität Stuttgart, Pfaffenwaldring 27, 70569 Stuttgart, Germany; hilfer@icp.uni-stuttgart.de*

Rudolf Hilfer is a professor at the Institute for Computational Physics at the University in Stuttgart, Germany.

ACKNOWLEDGEMENTS

We thank Statoil ASA and Numerical Rocks AS for granting permission to publish this work. We thank the Australian National University for acquisition of the microtomograph images and to Tony Boassen for the scanning electron microscope and backscattered electron microscope images, providing valuable microscale information indispensable for this study. Comments and support by Arve Lønøy, Carl Frederik Berg, and Arnout Colpaert are gratefully acknowledged. Special thanks to Stig Bakke for patiently briefing the first author regarding continuum-based modeling and list-based modeling.

The computations were conducted at the Institut für Computerphysik, Universität Stuttgart, and the Scientific Supercomputing Center Karlsruhe (Rechenzentrum Karlsruhe). We are grateful to the Scientific Supercomputing Center Karlsruhe for computing time and technical support. The valuable reviews of this article by D. C. Kopaska-Merkel, J. Lucia, and R. P. Major are greatly appreciated.

The AAPG Editor thanks the following reviewers for their work on this paper: David C. Kopaska-Merkel, Jerry Lucia, and R. P. Major.

the model. The pore-size analysis and percolation tests performed in three dimensions at various discretization resolutions indicate pore-throat radii of 1.5 to 6 μm for the largest interconnected pore network. This also highlights the challenge to determine appropriate resolutions for x-ray imaging when the exact rock microstructure is not known.

INTRODUCTION AND BACKGROUND

The goal of pore-scale rock modeling is to gain a better tool for reservoir rock characterization. It is crucial to understand and quantify the impact of geologic parameters during rock genesis on the appearance and petrophysical properties of a rock. Relating geomodels (geology) to petrophysical parameters and flow characteristics, integrating geologic descriptions, petrophysical analyses, and reservoir engineering is a complex task, especially in the case of carbonate rocks.

The depositional environment and commonly multifold syndepositional and postdepositional diagenetic processes can create a vast variety of carbonate rock fabrics and pore structures. Methods and nomenclatures had to be introduced to describe and classify carbonates as they appear today after diagenetic overprinting.

Initial attempts of carbonate rock classifications were focused on establishing a common terminology among geoscientists. Folk (1959, 1962) based the classification on the grain types, their relative abundance, and ratio of microcrystalline matrix versus pore space (or cemented primary pore space). A classification of carbonate rocks according to the depositional texture, the grain-matrix relationships, and mud content was introduced by Dunham (1962), which was later modified by Embry and Klovan (1971), considering biogenic deposits such as reefal components. Wright (1992) combined both approaches and added diagenetic aspects to the Dunham (1962) and Embry and Klovan (1971) classification.

To close the gap between geologic description, petrophysics, and flow parameters, classification of the pore systems came into focus, especially for hydrocarbon exploration.

The porosity distribution in carbonate rocks is complex both genetically and physically. Interparticle, intraparticle, and diagenetically built pores, such as moldic and intercrystal pores commonly form dual or multiple pore systems, which can cover several orders of magnitude in size. The combination and fractional contribution of individual pore systems, from microporosity up to centimeter-size molds, forming the multiple pore system will determine the petrophysical properties of the

carbonate rock and thus the performance with respect to hydrocarbon production.

Choquette and Pray (1970) introduced a classification into basic pore types according to fabric selective, or not fabric selective, specified by genetic modifiers. Whereas this classification is helpful to relate individual pore types to depositional environments and diagenetic alteration, it is difficult to achieve a relationship to flow properties in a three-dimensionally interconnected pore system.

Lucia (1983, 1995, 1999) presented an approach to define petrophysical rock classes based on carbonate rock fabrics and the corresponding pore systems from visual description. Later, the concept of constructing flow units based on rock fabrics, petrophysical properties, and pore-throat-size distributions was shown to be beneficial for more accurate reservoir characterization (Kerans et al., 1994; Martin et al., 1997; Aguilera, 2002, 2004).

Connecting empirical porosity-permeability relations to the sedimentologic and diagenetic rock descriptions, Lønøy (2006) introduced a new pore-type classification system. This classification consists of 20 pore-type classes and allows a better description of mixed pore geometries (variations in both pore shape and pore size).

Direct imaging of the rock via x-ray microtomography (MCT) is a promising approach that results in a three-dimensional (3-D) representation of the rock framework and the pore network and allows numerical computations of petrophysical properties and fluid-flow properties. However, because MCT imaging must be capable of resolving microfeatures and connectivity present in the rock pore network, it is to be performed at sufficiently high resolution. This, because of computational restrictions, reduces the manageable sample sizes to a few millimeters or less. This resolution-versus-size problem is a general challenge for rock modeling or reconstructions, such as the process-based rock modeling for sandstones (Bakke and Øren, 1997; Øren and Bakke, 2002) or stochastic modeling (Adler et al., 1990; Hazlett, 1997; Hilfer, 2000; Manwart et al., 2000; Biswal et al., 2007). Such modeling techniques and extraction of petrophysical properties, including single-phase flow, have

already been applied to a dolo-grainstone by Bakke et al. (2007) and Biswal et al. (2007, 2009a, b) and to sandstone in Latief et al. (2010).

The traditional way to gather petrophysical information and flow parameters of reservoir rocks is to perform laboratory measurements. However, core analyses are time consuming and it can be destructive for the sample material, especially when dealing with weakly consolidated material or soluble carbonates. Moreover, undisturbed core plugs are required.

The advantages of generating numerical rocks by rock modeling are multifold. It is a time-saving, nondestructive, and easily reproducible procedure. Rock models are readily modified to study the impact of geologic heterogeneity (modifications of rock components) on petrophysical parameters. Its drawback, however, is the replacement of the exact microstructure by an approximate model.

Whereas a dual or multiple scale rock modeling approach for carbonate rocks (Ghous et al., 2008; Wu et al., 2008) provides a partial solution to the resolution-to-volume challenge, it has not been possible to represent continuous multiscale information in a single rock model.

The approach used herein follows the approach introduced in Biswal et al. (2007, 2009a, b). It aims to combine the advantages of direct imaging using MCT and rock modeling to include rock and pore-space information from microscale to macroscale into one single continuum-based rock model. This approach tackles the resolution-versus-size challenge in decorating a large MCT volume at a low resolution (achieving a considerable volume) with microscale information from thin sections, scanning electron microscope (SEM) images, and back-scattered electron (BSE) microscope images. This procedure results in a large sample volume in the range of core plugs that may contain rock information more than four orders of magnitude in size. The continuum model is subsequently discretized at any desired resolution for investigation of the contained pore systems (Latief et al., 2010). Petrophysical property calculations and flow simulations on the rock models could in turn be linked directly to pore typing and a petrophysical property-related carbonate classification, which is beyond the scope of this contribution.

MATERIALS AND METHODS

Data Availability

Along with a thin section of the carbonate core plug, 3-D MCT volumes at three different resolutions (42, 5.6, and 2.8 $\mu\text{m}/\text{voxel}$) were available for the sample characterization. In addition, a series of BSE and SEM images with magnifications ranging from 40 to 1600 times was used to derive information on dolomite fabrics, crystal shapes, and crystal sizes down to submicron resolution.

Rock Description

The modeled dolostone is a biomoldic dolowackestone to packstone, exhibiting polymodal replacement fabrics (Figure 1). The biomolds are partly filled by aphanocrystalline to very fine euhedral dolomite crystals (Figures 2, 3). The former micrite matrix is completely replaced by dolomite and has different types of dolomite fabrics: tightly packed mostly xenotopic texture and areas of idiotopic dolomite crystal fabrics (Figure 3). Anhydrite patches of up to 2.5 \times 0.8 mm are present in the plug, replacing carbonate and filling pore space. Most of the solution-enlarged biomolds are lined by dolomite rims consisting of

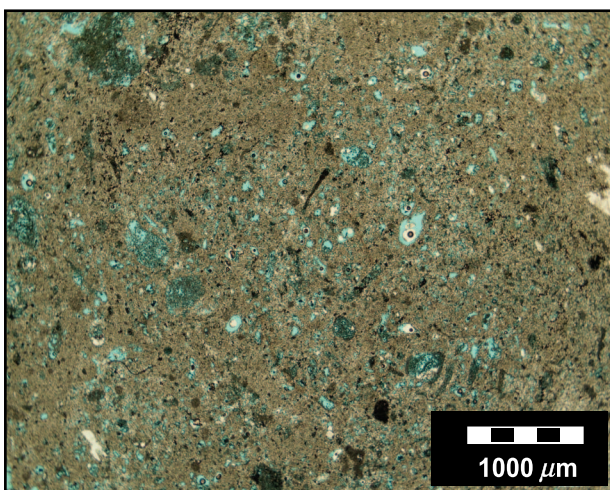


Figure 1. Thin section of the modeled dolostone sample. Brown colors indicate different dolomite matrix fabrics, light blue areas are open and partly crystal-filled biomolds, and white is anhydrite. Black colors might indicate organic remainders. Scale bar = 1 mm.

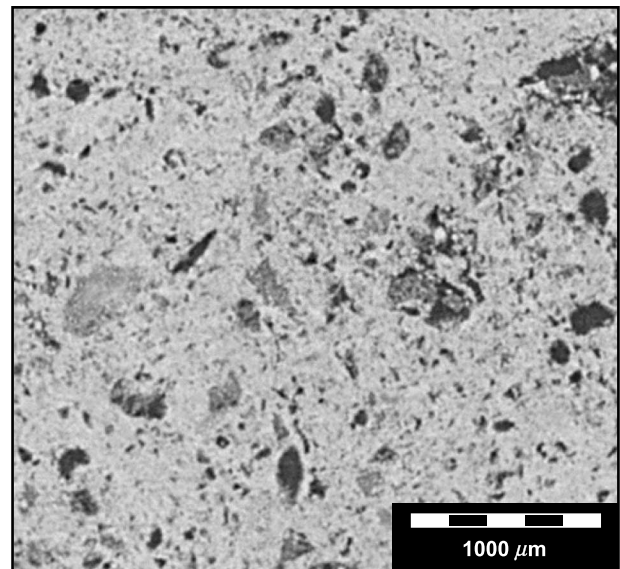


Figure 2. Two-dimensional slice of 5.6- μm resolution microtomograph illustrating open biomolds (black) and dolomitized former bioclasts (dark-gray). Light-gray areas depict different fabrics of dolomite matrix. Scale bar = 1 mm, side length = 3.2 mm.

fine euhedral dolomite crystals (Figure 4). The pore system ranges from intercrystalline microporosity to large mesoporosity. All rock parameters are derived from the thin section and from available BSE and SEM images.

Preparation and Preprocessing of the Microtomography

The low-resolution MCT had an original size of 600 \times 600 \times 200 voxels with a voxel size of 42 μm , corresponding to 2.52 \times 2.52 \times 0.84 cm side lengths. A representative subsample of 200 \times 200 \times 20 voxels was selected for model implementation. With a voxel size of 42 μm , many details of the microstructure (crystals and intercrystal porosity) present in the rock are not resolved. However, different rock phases contributing to the rock fabric can be clearly distinguished in the gray-scale MCT image.

In the absence of a properly defined term (the widely used term “facies” mainly applies to the appearance or nature of one part of a rock body as contrasted with other parts), the term “rock phase” is introduced. It was called “primordial phase” in a previous work of Biswal et al. (2007, 2009a, b).

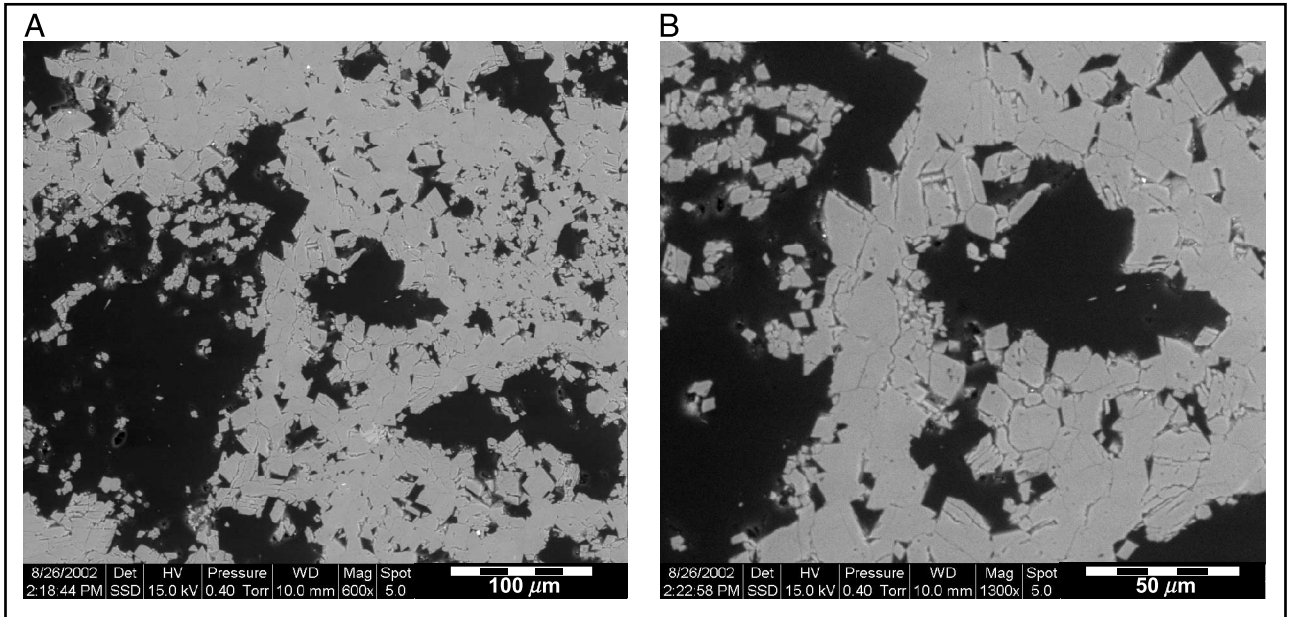


Figure 3. Backscattered electron microscope images illustrating the individual dolomite fabrics described in the text (gray colors). Areas of xenotopic dolomite fabric alternate with well-crystallized very fine to fine dolomite crystals. Aphano to very fine size dolomite crystals occupy parts of the molds. Scale bars = 100 (A) and 50 μm (B).

“Rock phase” herein refers to a separate region of the rock with distinct types of mineralogy and crystal properties (such as habitus, size, orientation, and packing) or differences in porosity. Different precursor bioclast types, open or filled pore space, and matrix differences caused by varying amounts of

microporosity and dolomite crystal habitus leave their imprint on the local density and thus on the gray values of the MCT. Following this schematic, the subsample was segmented into six recognizable rock phases (Table 1). To gain realistic molds-to-dolomite matrix boundaries (because of the

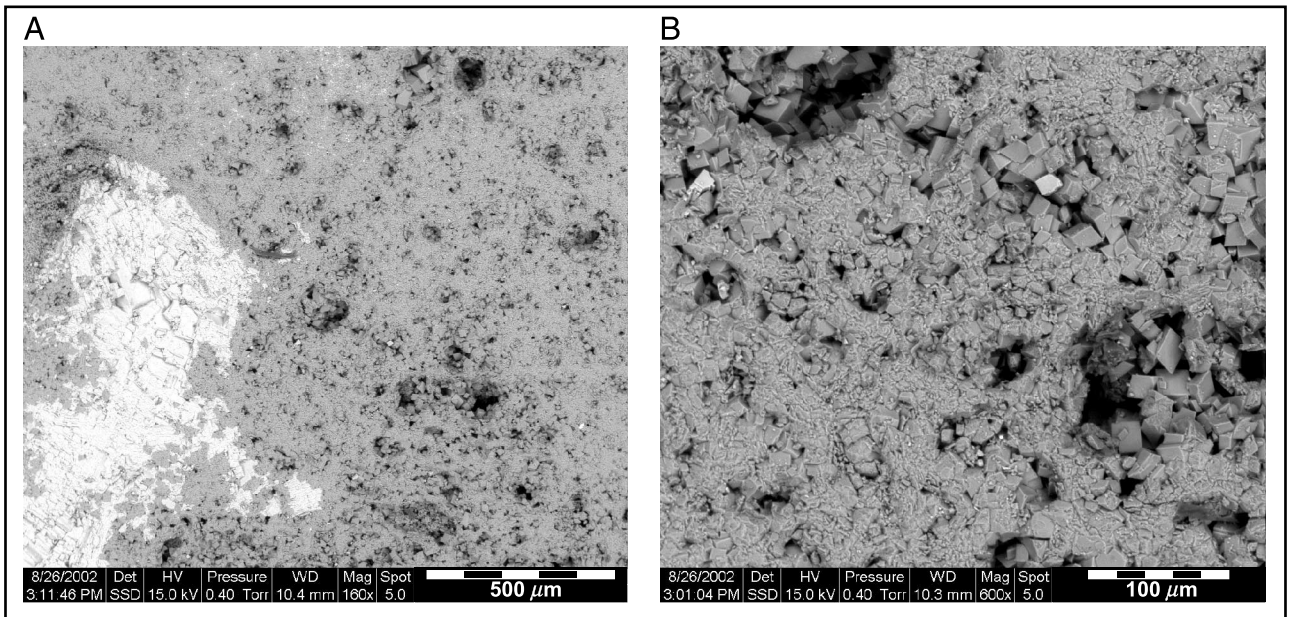


Figure 4. Scanning electron microscope images showing anhydrite areas (white, A) and euhedral fine dolomite crystals making up the rims and lining the molds (B). Scale bars = 500 (A) and 100 μm (B).

Table 1. Differentiated Rock Phases and Porosity Budget of the Primordial

Rock Phase	Volume* (%)	Crystal Sizes		
		(c axis in μm)	ϕ^{**} (%)	$\phi_{\text{total phases}}^{\dagger}$ (%)
Phase 1: anhydrite	10.2	10–80	1.0	0.1
Phase 2A: matrix, xenotopic (mixture of xenotopic and idiotopic)	48.1	5–38	14.5	7
Phase 2B: matrix, idiotopic	18.6	14–30	18	3.4
Phase 3: rims, idiotopic	17.9	20–53	35	6.3
Phase 4: molds, filled idiotopic	0.6	3–12	50	0.3
Phase 5: open molds	4.5	–	100	4.5
			$\phi_{\text{total rock}}$	21.5

*Volume percentages were derived from the primordial volume, crystal sizes, and microporosities of the individual phases from examination of the high-resolution SEM and BSE images.

** ϕ (column 4) is the porosity present in the individual rock phases.

$\dagger\phi_{\text{total phases}}$ (column 5) depicts the porosity contribution of the individual rock phases to the total rock porosity $\phi_{\text{total rock}}$.

coarse resolution, the boundaries were unrealistically “pixely”) the resolution was doubled and the volume was filtered with a standard Gaussian filter using a radius of 1.5. The resulting volume, hereafter referred to as primordial volume, had $400 \times 400 \times 40$ voxels with a voxel size of $21 \mu\text{m}$, corresponding to a volume of $8.4 \times 8.4 \times 0.84$ mm side length. This primordial volume was used for the model generation, as explained below.

Modeling Procedure

The dolomite rock is represented by a list of crystals defined geometrically. Each of the observed

rock phases is characterized by distinct crystal properties, such as type, size, overlap, and orientation (Biswal et al., 2007, 2009a, b). The list of crystals representing the rock is created by depositing them separately for each of the rock phases and then combining them. In each phase, these crystals are deposited in a random sequence and correlated with the texture of the original rock sample illustrated in Figure 5 and described in Table 1.

Mathematically, the rock occupies a bounded region in space, and each element of the list is numbered by an index i . It represents a crystal at position $x_{i,j}$, associated inscribed sphere of radius

Figure 5. Color-coded 2-D slice of the segmented $21\text{-}\mu\text{m}$ resolution primordial volume used for modeling. Open molds are light blue, fine crystalline dolomite rims of molds are green, gray areas depict aphanitic to very fine crystalline dolomite-filled molds, and dark blue and purple are the former matrix replaced by very fine to fine idiotopic and xenotopic dolomite fabrics, respectively. White patches are anhydrite. The primordial volume has a side length of $8.4 \times 8.4 \times 8.4$ mm. The colors are chosen arbitrarily and represent different gray shades in the MCT. Scale bar = 1 mm.

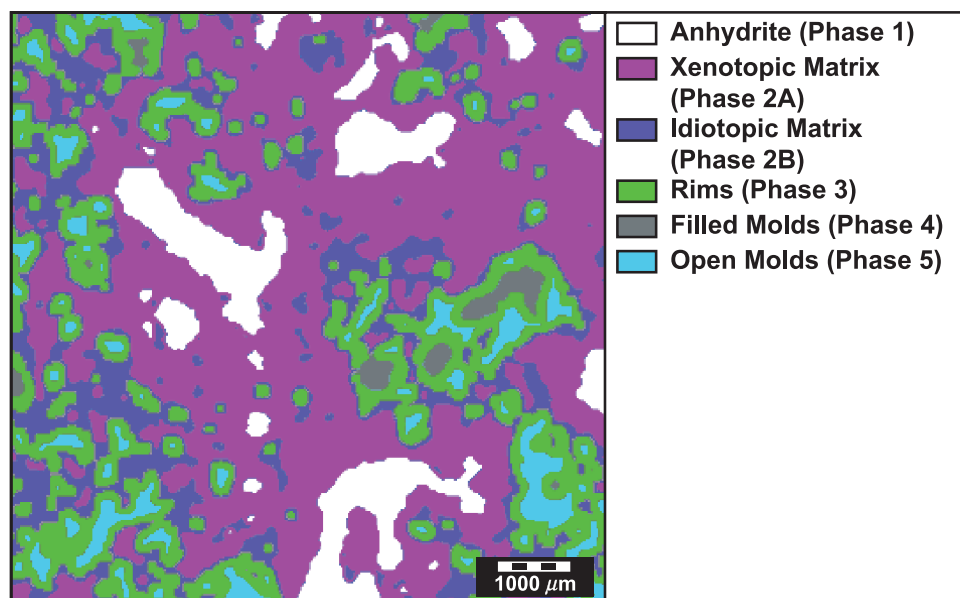


Table 2. Model Parameters for Each Rock Phase Containing Solids

Rock Phase	R_{\min}^* (μm)	R_{\max}^* (μm)	Maximum Overlap**	Orientation [†] (°)	No. Crystals ^{††}
Phase 1: anhydrite	2.5	20.0	0.7	x: -20, -20 y: -20, -20 z: -25, -5	1,281,132
Phase 2A: matrix, xenotopic: idiotopic fraction	3.5	9.5	0.2	(-90, 90)	28,831,185
space filling xenotopic fraction	1.25	3.5	0.5	(-90, 90)	76,020,321
Phase 2B: matrix, idiotopic	3.5	7.5	0.2	-90, 90	15,132,127
Phase 3: rims, idiotopic	5.0	13.25	0.2	-90, 90	3,199,305
Phase 4: molds, filled idiotopic	0.75	3.0	0.2	-90, 90	2,906,304
				Total	127,370,374

* R_{\min} and R_{\max} are the minimum and maximum radii of the associated sphere at each point of the sequence.

**The overlap between two spheres is defined by $(R_i + R_j - |x_i - x_j|) / (R_i + R_j + |R_i R_j|)$. The minimum overlap is assumed zero.

†The orientation of the crystals is specified by three sequential rotations about the three coordinate axes chosen randomly from the interval given in the fifth column (orientation).

††The number of crystals deposited for the respective rock phases.

R_i , orientation a_i , and type T_i . The position x_i is a 3-D vector, the radius a positive real number, the orientation a_i is a unit vector on the unit sphere, and the type is an integer from $\{1, \dots, N\}$. These attributes are correlated with the texture of the rock through a carefully constructed grayscale filter function $G(x)$ (Figure 5). For this model implementation, the filter function $G(x)$ is constructed from the low-resolution MCT image (the primordial volume). Because different rock phases present in the MCT are represented by different grayscale intervals, the grayscale value $G(x)$ determines the type and properties (size, orientation, and overlap with neighboring crystals) of the crystal that can be placed at position x . If $G(x) = 0$ at position x , it represents pore space including the moldic pores, and no deposition of crystal is allowed at x .

For each rock phase, a list is generated by randomly selecting a position x_i and an associated sphere of radius R_i is chosen randomly from the interval (R_{\min}, R_{\max}) . Each entry of the list has to satisfy two additional constraints. First, a fully supported matrix is achieved by ensuring that each added crystal has a finite overlap with at least one of the existing crystals (Biswal et al., 2009b). The degree of allowed overlap at a point x depends on the rock phase and is specified through $G(x)$. This way, the packing of crystals in each rock phase correlates with the textural features of the rock. Second, the target porosity of the crystal packing in each rock phase is ensured by depositing crystals

with a specific point density, as well as specified through $G(x)$ (Biswal et al., 2009b).

This modeling procedure results in a volume of the rock that is fully represented by a list of N quadruples (x_i, d_i, a_i, T_i) . The crystals are geometrically defined objects in the continuum, and the size d_i should be such that it inscribes the associated sphere of radius R_i . This retains the matrix connectivity. The model parameters for each of the rock phases and the number of crystals needed to specify each rock phase within the modeled volume of the rock are summarized in Table 2.

Synthetic Computed Tomography

The continuum model described in the previous section can now be discretized at any desired resolution. To this end, the continuum model is divided into a grid of cubic voxels. In each voxel n^3 , collocation points are placed symmetrically onto an $n \times n \times n$ cubic sublattice. A grayscale value $0 \leq m \leq n^3$ is then assigned to each voxel, where m is the number of collocation points that fall inside the crystal matrix (Biswal et al., 2009b).

The resulting grayscale grid represents a synthetic MCT image of the numerical rock model at the selected voxel resolution (Biswal et al., 2009a). Such synthetic MCT images can be created at any arbitrary resolution, only limited by available computational resources. They can be used for microstructure characterization, prediction of transport

parameters at intermediate resolutions, and extrapolation of transport properties to even higher resolution than the originally available data (Biswal et al., 2007).

Model Implementation

Model parameters (Table 2) are adjusted to achieve the targeted porosity and crystal packing in each phase. The continuum list representing the rock requires deposition of millions of overlapping poly-disperse crystals. Each point in the list is then decorated by crystals defined geometrically, as follows.

The idiotopic dolomites are represented by equilateral rhombohedra. Each rhombohedron (before rotation) centered at x_i is defined by the intersection of three pairs of parallel planes. Each pair is separated by a distance $d_i = 2 \times R_i$ and tilted by an angle $\alpha = -15^\circ$ about the coordinate axes to which they were parallel initially (Biswal et al., 2009b). The xenotopic dolomites are defined by adding 12 to 18 randomly oriented cutting planes to the equilateral rhombohedra defining the idiotopic dolomites. The crystals in the bioclast phase are represented by idiotopic dolomites. The crystals in the anhydrite phase are represented by rectangular parallelepipeds with side lengths in the ratio 1:1:2. Biomolds were identified from high-resolution images and modeled by removal of crystals. These biomolds form linearly extended paths or tunnels and are clearly visible in high-resolution SEM images but unresolved in the low-resolution MCT. Approximately 1.27×10^8 geometric objects represent the final rock model. The model is then discretized by placing and testing $n^3 = 216$ collocation points inside each voxel.

RESULTS AND DISCUSSION

Modeling of Rock Fabrics

Before the modeling procedure, the primordial volume was segmented into six different rock phases (see Table 1):

Next to the open (solution enlarged) molds (phase 5), the rock can be subdivided into five dia-

genetic phases: anhydrite (phase 1), former matrix replaced by a mixture of xenotopic and idiotopic dolomite fabric (phase 2A) and purely idiotopic fabric (phase 2B), cement rims lining the molds (phase 3), and molds that have been completely filled by euhedral dolomite crystals (phase 4). Figure 5 shows a two-dimensional (2-D) slice cut through the 3-D volume, illustrating the segmentation into the six phases. Whereas the overall distribution into the rock phases was obtained from the primordial volume (Figure 5), the microscale information of the individual rock phases was derived from high-resolution BSE and SEM images (Figures 3, 4).

The anhydrite (phase 1) consists of densely packed orthorhombic crystals 5 to 40 μm in diameter with negligible intercrystalline microporosity (compare Figure 4) and makes up approximately 10.2% of the primordial volume. With a volume fraction of 48.1%, the xenotopic dolomite phase 2A (mixture of xenotopic and idiotopic dolomite) occupies the major part of the former matrix space. Individual crystal sizes range from 5 to 38 μm (c axis), and the average intercrystalline porosity amounts to 14.5%. Idiotopic dolomite replaces the rest of the primary matrix (phase 2B; approximately 18.6%). Crystal sizes range from 14 to 30 μm (c axis), and this phase has an average porosity of 18%. The largest idiotopic dolomite crystals, 20 to 53 μm (c axis), are found to line the molds (phase 3; 17.9 volume %), the smallest, only 3 to 12 μm , are found in the entirely replaced former bioclasts (phase 4; 0.6 volume %). Intercrystalline porosities amount to approximately 35 and 50% for phases 3 and 4, respectively.

The parameters derived from the high-resolution images, such as crystal sizes, microporosity, crystal density/overlap, and crystal orientations, were used to model the individual rock phases of the primordial volume. The result of this rock modeling procedure is an artificial rock that has the rock-phase distributions and the volume of the primordial volume ($8.4 \times 8.4 \times 0.84$ mm side length) and at the same time carries the high-resolution information of the SEM and BSE images at a micrometer scale. Table 1 presents an overview of the volume percentages, the crystal sizes, porosity of

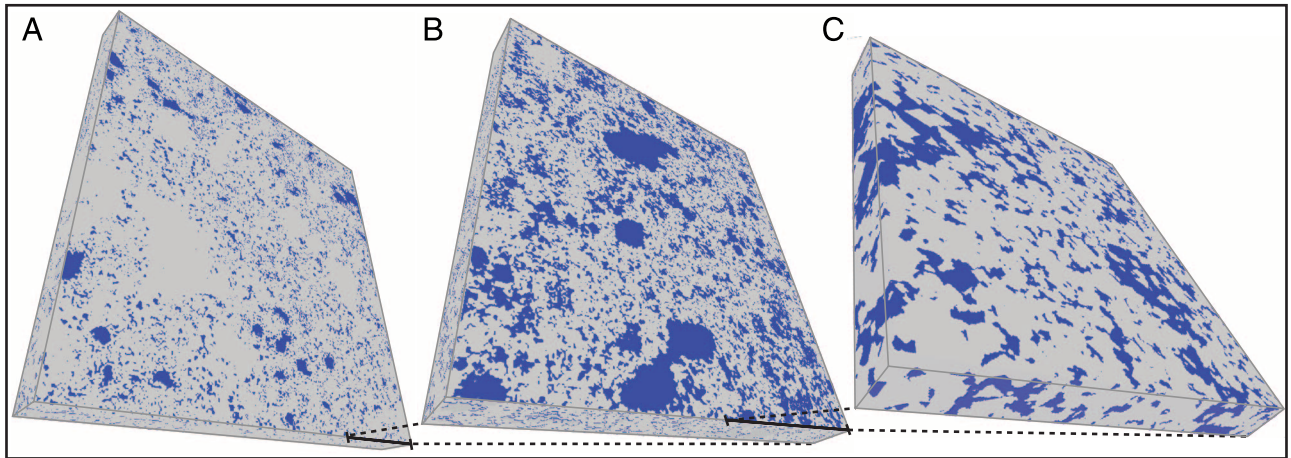


Figure 6. Modeled sample discretized at different resolutions. Blue is pore space, gray is dolomite. (A) 10.5 $\mu\text{m}/\text{voxel}$, horizontal width: 8400 μm ; (B), 1 $\mu\text{m}/\text{voxel}$, horizontal width: 1618 μm ; (C) 0.25 $\mu\text{m}/\text{voxel}$, horizontal width: 404.5 μm . With higher resolution, increasingly finer pore and crystal structures are resolved. While in the 10.5- μm discretization, only the macropores and molds are visible (A), macroscale and microscale intercrystal porosity is resolved in the 1- μm discretization (B), and only intercrystal microporosity is captured in the 0.25- μm resolved volume (C). Note that the discretizations were arbitrarily taken from different regions of the model and, therefore, textures differ. Corresponding sizes are indicated by the scale bars illustrating the resolution dependence of the pore distributions.

the individual rock phases, and the total porosity of the modeled rock volume.

The resulting model continuum was subsequently discretized at 0.25, 1, 2.625, 5.25, and 10.5- μm resolution. Figure 6 displays three different discretizations at 10.5, 1, and 0.25, illus-

trating captured volumes and resolved structures as a function of the resolution of the discretization. The 10.5- μm resolved model has the volume of the primordial volume and can grasp the moldic porosity and macroporosity. At 1- μm resolution of some smaller molds, macroporosity and microporosity

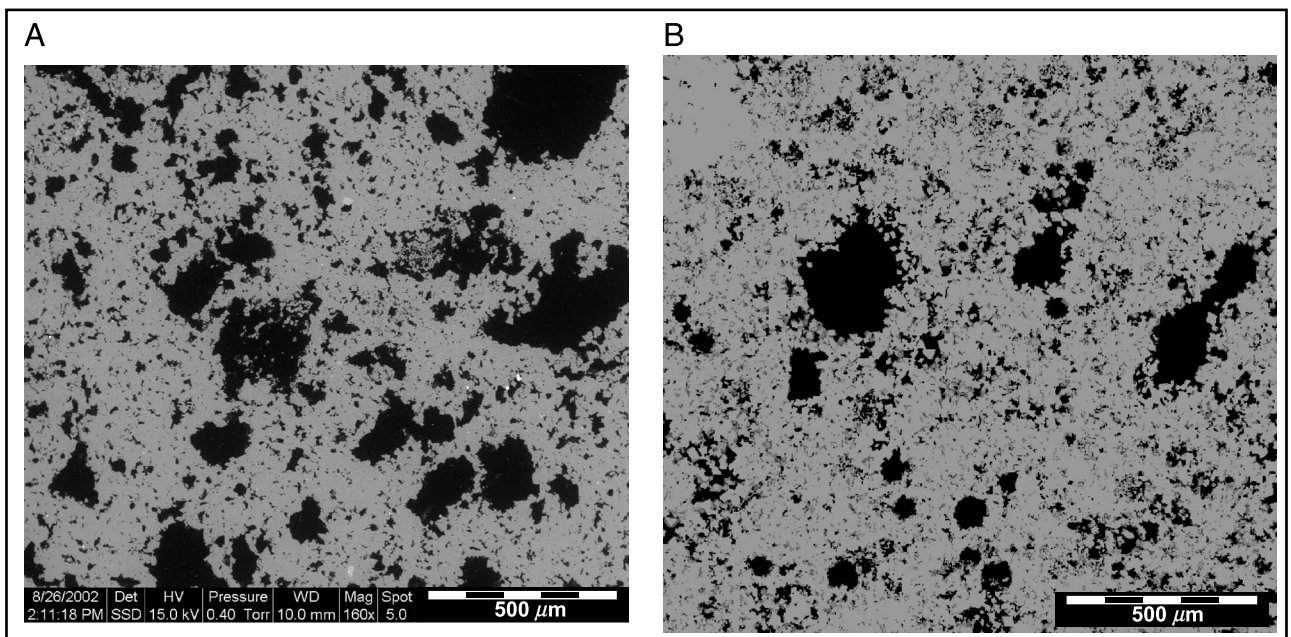


Figure 7. A BSE microscope image of original rock (A) (160 \times magnification, width 1597 μm , height 1347 μm) versus a slice (10 μm thickness) of the modeled rock (B) (width 1618 μm , height 1491 μm). Black is pore space, gray is dolomite. Scale bar = 0.5 mm. Both images are to scale and directly comparable.

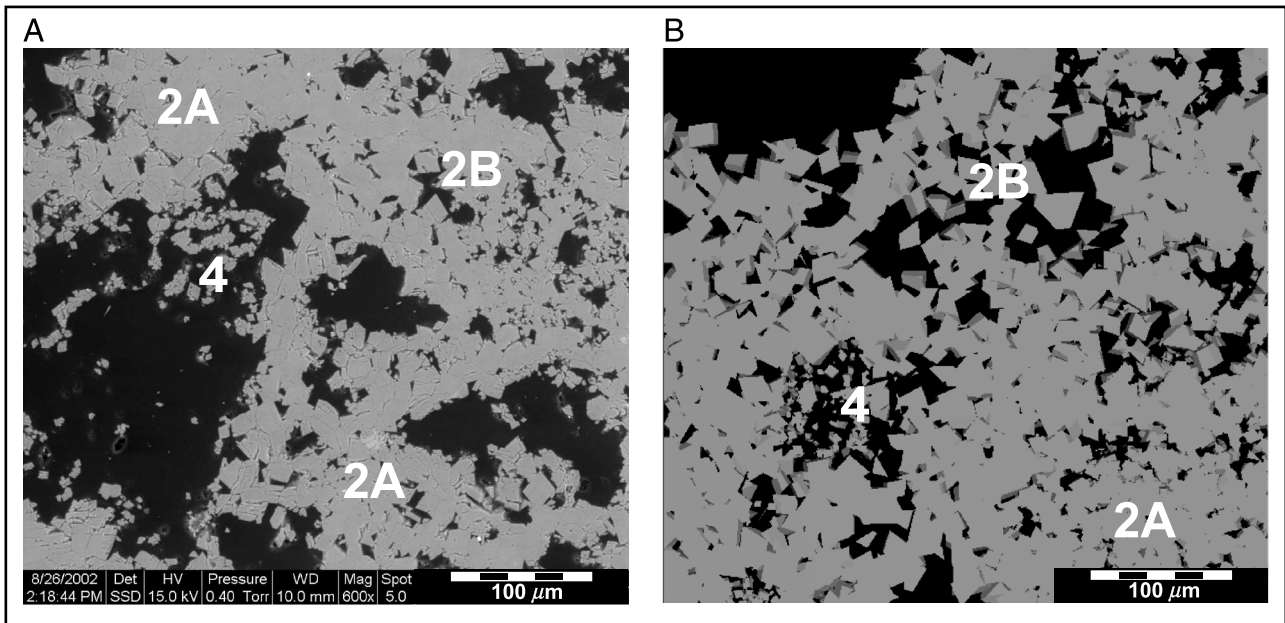


Figure 8. A BSE microscope image of the original rock (A) (600× magnification, width 432 μm, height 399 μm; black is pore space, gray is dolomite) versus a 2-D slice (5 μm thickness) of the modeled rock (B) (width 432 μm, height 398 μm). Black is pore space, gray is dolomite. Areas of denser packed mostly xenotopic dolomite fabrics (2A), areas of higher porous idiotopic dolomite fabrics (2B) and aphanocrystalline dolomite occupying the molds (4) can be identified in both images. Scale bar = 0.1 mm. Both images are to scale and directly comparable.

are resolved. Pores and dolomite crystals down to submicrometer size are captured when discretizing the model at a 0.25-μm resolution, whereas a single

intermediate-size mold of approximately 400 μm would occupy the entire discretizable volume at that resolution (Figure 6).

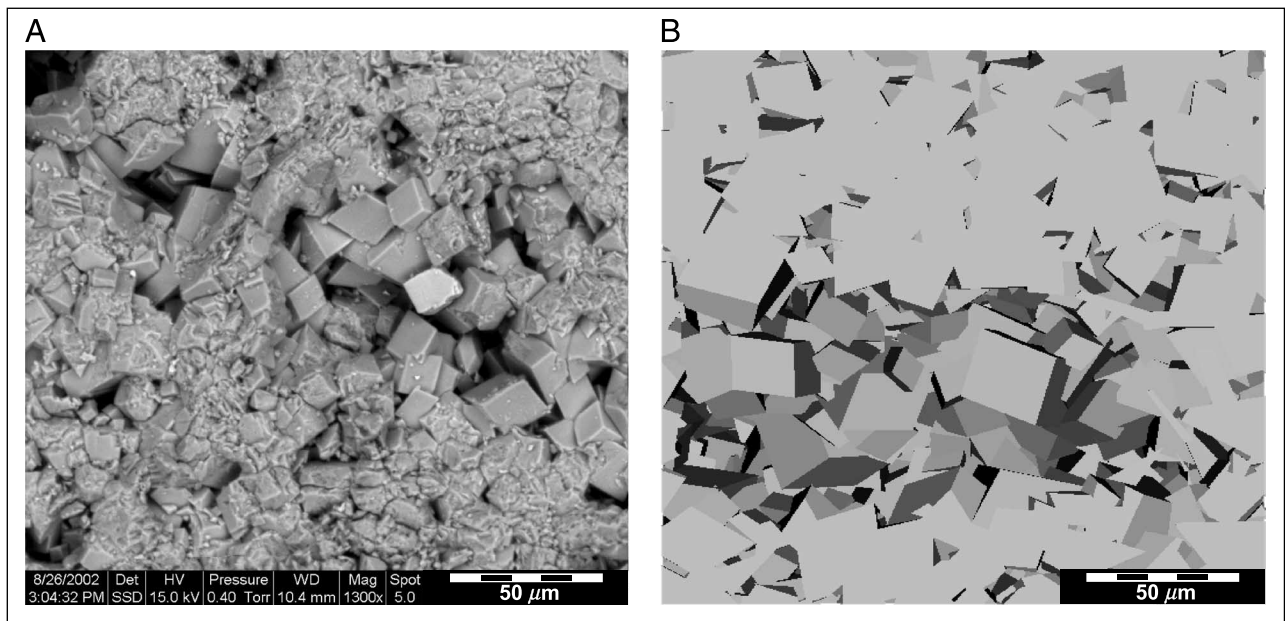


Figure 9. An SEM image of original rock (A) (1300× magnification, width 200 μm, height 184 μm) versus a 2-D slice (50 μm thickness) of the modeled rock (B) (width 200 μm, height 184 μm). Black is pore space, gray is dolomite. Scale bar = 0.05 mm. Both images are to scale and directly comparable.

Table 3. Different Discretizations of the Model, MCTs, and BSE Images Used for the Pore-Size Analyses*

Image	Resolution ($\mu\text{m}/\text{voxel}$ or pixel)	Image Size (mm)
Model	10.5	$8.4 \times 8.4 \times 0.84$
	5.25	$8.4 \times 8.4 \times 0.84$
	2.625	$8.4 \times 8.4 \times 0.84$
	1	$1.6 \times 1.5 \times 0.2$
	0.25	$0.4 \times 0.4 \times 0.05$
MCT	42	$21 \times 21 \times 8.4$
	5.6	$2.8 \times 2.8 \times 2.8$
	2.8	$2.8 \times 2.8 \times 1.4$
BSE	6.33	4.2×4.4
	1.58	1.6×1.4

*MCT = microtomograph; BSE = backscattered electron.

Sizes and distribution of individual dolomite fabrics and porosity types in the model can be well illustrated and compared with the original BSE and SEM images using 2-D slices of the discretized volumes. Figures 7–9 illustrate direct comparisons between BSE and SEM images of the original rock and 2-D slices taken from the 3-D models at different discretizations. Molds and macroporosity are well resolved in the BSE image at 160 \times magnification. This is illustrated by the 2-D slice of the model at a corresponding resolution (Figure 7). The sizes of the images are almost

identical, so that structures are approximately to scale and directly comparable. Vug sizes, shapes, and distribution, as well as macroporosity visible in the BSE image, are reproduced by the model. Differences in dolomite matrix density in both images mirror the different dolomite fabrics: the higher microporous idiotopic fabrics of phase 2B and the denser lower porosity xenotopic-idiotopic mixture phase 2A. This becomes more evident at a higher resolution, as illustrated in Figure 8. Both images, BSE and model, have identical side lengths. Areas of denser packed, mostly xenotopic dolomite fabrics (phase 2A) and areas of higher porous idiotopic dolomite fabrics (phase 2B) can be identified. Moreover, some smaller dolomite crystals within the molds (phase 4) can be seen in both images. The SEM image (Figure 9) allows a more 3-D insight into the dolomite appearance of the rims lining the molds (phase 3).

Overall, the comparison between the model at different resolutions and original BSE and SEM images shows that the fabric of the rock is well captured in the model at all length scales.

Pore-Size Distribution

The rock fabric defines the pore network, which in turn determines the petrophysical flow characteristics. The pore systems of the modeled rock

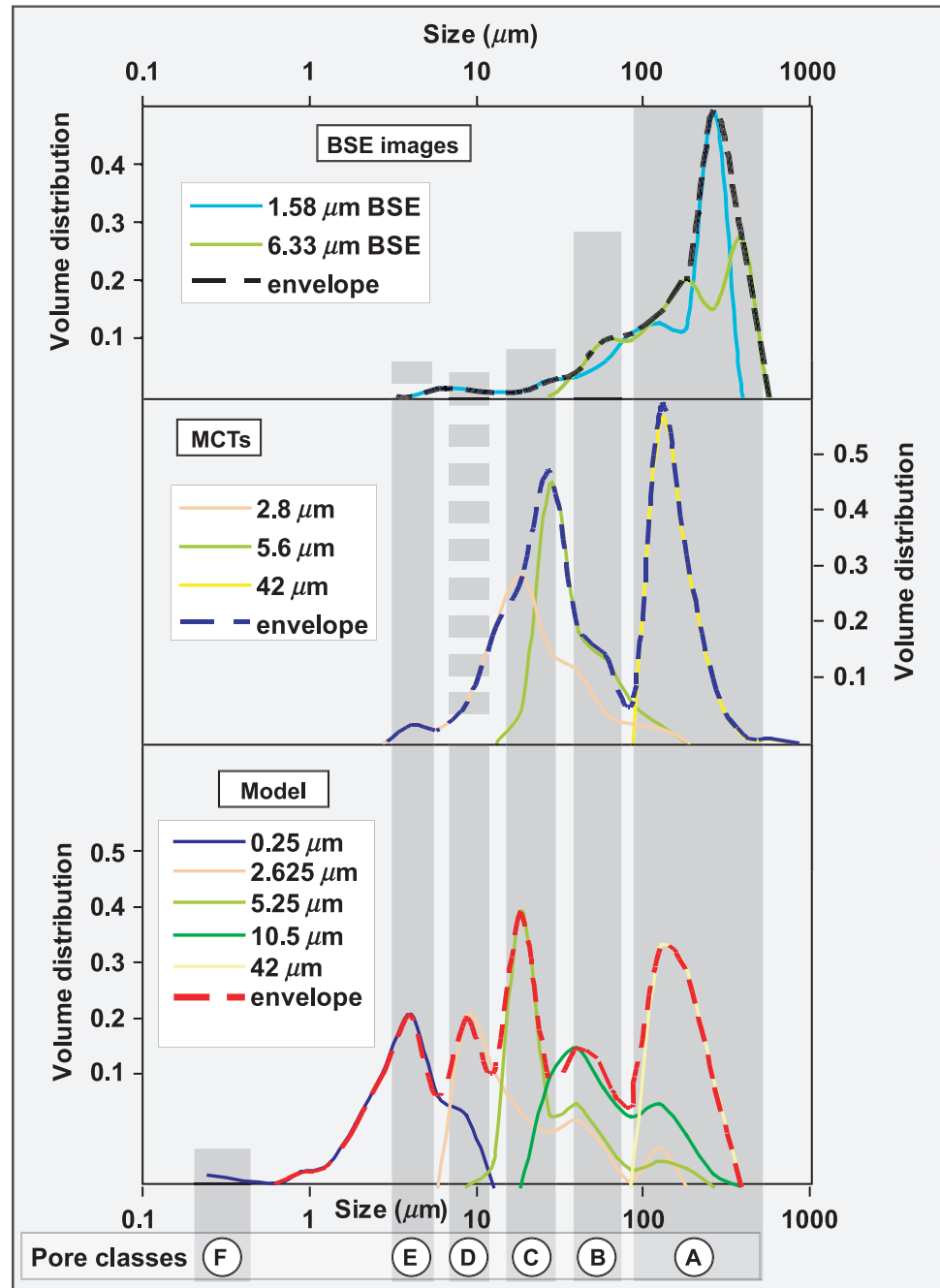
Table 4. Pore Classes Present in the Modeled Rock

Pore Classes (this study)	Pore Sizes (μm)	Vol. %* (of ϕ_{total})	Pore Class Percolating	Pore Origin/Distribution	Pore Class (Lønøy, 2006)	Petrophysical Class** (Lucia, 1995)
A	>100	32	No	Rock phase 5; (solution enlarged biomolds)	Moldic macropores	SV
B	35–80	15	No	Rock phases 4 and 5 (smaller molds)		
C	15–25	25	No	Rock phases 3 and 2B	Intercrystalline micropores and mesopores	IP, class 2/3: fine to medium crystalline mud-dominated dolostone
D	8–12	13	?	Rock phases 2A and 2B	Mudstone micropores	IP, class 3: fine crystalline mud-dominated dolostone
E	3–5	14	Yes			
F	<1	<1				

*Vol. % (of ϕ_{total}) in column 3 gives the volumetric contribution of the individual pore classes to the overall porosity.

**SV = separate vug porosity; IP = interparticle porosity.

Figure 10. Comparison of pore volume distributions from (BSE) microscope images (upper panel), original microtomographs (MCTs) (middle), and model at different discretizations (lower panel).



were investigated and compared with the analyzed pore systems of the original MCTs and the 2-D BSE images. A maximum ball algorithm (Silin and Patzek, 2006) was used to perform pore-size analyses. Because this method does not discriminate between pore bodies and pore throats, the terms “pore class” or “pore size” within this study include pore-throat sizes. The pore sizes were determined on five discretizations of the model (0.25, 1, 2.625, 5.25, 10.5- μm resolutions), on three differently re-

solved MCTs (2.8, 5.6, and 42- μm resolutions), as well as on BSE images at 1.58 and 6.33 μm pixel sizes (Table 3). Four times the resolution (voxel per pixel size) was chosen as the lower cutoff value for the maximum ball algorithm. Exceptions were the pore-size analyses at highest resolutions (0.25 μm for the model and 2.8 μm for the MCT), where no cutoff parameter was applied. This allows detection of the smallest pores that can be resolved at the highest resolution (pore class F for the model, class

D for the MCT; Table 4; Figure 10). Mudstone microporosity class F ($<1\ \mu\text{m}$) is typically not important for fluid flow in open pore systems and would contribute only little to the saturation budget of this rock type. Nevertheless, class F is included here to demonstrate no resolution restriction for the continuum model at the lower end of the pore-size distribution. Moreover, this class F microporosity may have a large impact on water saturation in many limestone reservoir rocks. The resulting pore sizes from the 2-D BSE images were corrected to 3-D sizes (Sahagian and Proussevitch, 1998) to allow for comparison with the 3-D sizes of the MCTs and the individual discretizations of the model.

Six pore-size classes are distinguishable in the model (Figure 10). Table 4 gives an overview of the pore-size classes, their distributions, and corresponding pore classification from Lønøy (2006), and for comparison, the petrophysical classes according to Lucia (1983, 1995, 1999). The Lucia (1983, 1995, 1999) petrophysical classes are defined by dolomite crystal size instead of pore sizes. For this study, the pore classification of Lønøy (2006) is most appropriate and will be followed for the rest of this article.

The largest pore class (A) ranges from 100 to 500 μm in diameter and is made up of biomolds and solution-enlarged biomolds. Pore class B encloses pores in the range of 35 to 80 μm in size and is related to smaller molds and partly filled molds in the model. Pore classes A and B originate from the model phases 5 and 4 (molds or solution-enlarged biomolds, Table 1) corresponding to the pore class moldic macropores of Lønøy (2006). Pore class C has a size range of 15 to 25 μm in diameter and may originate from rock phase 3 (rims, lining the molds) and the more loosely packed matrix phase 2B. This pore class C corresponds to intercrystalline mesopores and micropores. Pore classes D (8–12 μm), E (3–5 μm), and F ($<1\ \mu\text{m}$) fall into the pore class mudstone micropores (Lønøy, 2006).

Overall, the pore classes analyzed from the model span four orders of magnitude in size, which can arbitrarily be expanded at the lower end ($<1\ \mu\text{m}$) by discretizing the model at an even higher reso-

lution ($<0.25\ \mu\text{m}/\text{voxel}$). The model resolves the full range of pore sizes present in the rock, from moldic macropores, over intercrystalline macroporosity, mesoporosity, and microporosity to different size classes of mudstone microporosity (Figure 10, lower panel; Table 4).

Pore-size analysis on the MCT volumes indicates moldic macropores (pore classes A and B), intercrystalline mesopores and micropores (pore class C), although pore class B seems to be slightly underrepresented. In addition, mudstone micropore classes D (subordinate) and E are captured (Figure 10, middle panel).

The investigated BSE images at 1.58- and 6.33- μm resolution (Figure 10, upper panel) contain all pore sizes from class A (moldic macropores) to class E (mudstone micropores). The slight shift in the pore classes with respect to the 3-D MCT and model volumes might be an effect of the sample cross section and applied 2-D to 3-D size correction. Note also that the pore-size information contained in 2-D images allows for porosity quantification, but it does not provide sufficient information on the interconnectivity of the pores systems in the third dimension.

Connectivity and Mean Pore-Size Class for Flow

Because the connectivity of a pore system is not known a priori, it is difficult to decide on a sufficient resolution for x-ray imaging, for example, whether for the studied rock type, the 5.6- μm -resolved MCT would be appropriate for petrophysical rock characterization. It might or might not cover the main connected pore-size classes governing the flow behavior. A series of percolation tests performed on the MCT volumes and on the different discretizations of the model provided information about the largest connected pore network.

Clearly, no connectivity is given for pore class A of the investigated dolostone sample in both the MCT data and the model. The connectivity of class B can be examined on the 10.5- μm resolution discretization of the model. At this resolution, only pore classes A and B are resolved, whereas pore classes C to F are below the resolution limit (Figure 10). The

percolation of the pore space was analyzed with an algorithm from Hoshen and Kopelman (1976). This analysis revealed that the model discretization at 10.5- μm resolution is not percolating, which indicates that pore classes A and B are different size classes of unconnected macromoldic porosity, the separate vug porosity of Lucia (1995). Together, they make up 47% of the total pore space, occluding 0.1 of the total porosity of 0.215 available for flow.

To test if pore class C (15- to 25- μm pore diameter) builds a connected pore system, percolation tests were performed on the 5.6- μm MCT and on the 5.25- μm discretization of the model. Whereas the MCT mainly resolves the upper range of pore class C and pore class B (only subordinately the large molds of pore class A), the model discretization at 5.25- μm resolution covers pore classes A and B and the full range of C. Neither the 5.6- μm -resolved MCT nor the model at 5.25 μm was shown to percolate. This indicates that pore sizes creating a connected pore network must be well below that of pore class C, the pore class that is captured by the 5.6- μm MCT and 5.25- μm model discretization, respectively (Table 4; Figure 10). This corroborates the skepticism expressed above, whether the 5.6- μm resolution MCT would be appropriate for a petrophysical rock characterization.

The pore systems of the 2.8- μm MCT and the 2.625- μm model discretization percolate indicated a connected pore system established at pore sizes corresponding to the mudstone micropore class D or E. Without petrophysical measurements, numerical simulations, or laboratory experiments, it is not possible to specify whether pore class D or E establishes the largest connected pore network in this rock. However, both pore classes are related to the rock matrix phases 2A and 2B (Table 4). With 48.1% in volume, the denser matrix phase 2A ($\phi_{2A} = 14.5\%$) covers more than 2.5-fold the rock volume occupied by the more loosely packed, higher porosity, matrix phase 2B, which occupies 18.6% of the rock volume (Table 1). Because of this phase-volume ratio, the less porous phase 2A contributes more than double the amount of the porosity available for flow compared with the more porous matrix phase 2B (7 vs. 3.4% of ϕ_{total} , Table 1). Moreover, the distribution of the

rock matrix phases displayed in Figure 5 suggests that main flow occurs through the dense matrix phase 2A, connecting the intercrystalline pores and the moldic pores. The maximum pore-size diameter allowing flow is thus below approximately 3 to 12 μm (pore radius, 1.5–6 μm), which suggests an expected absolute permeability range of 1 to 10 millidarcys—very important information when characterizing a reservoir rock in the absence of any laboratory measurement or numerical flow simulation.

The correspondence of the pore classes analyzed from BSE images, MCTs, and discretizations of the model demonstrates the power of this approach to reproduce complex reservoir rocks and obtain a representative multiscale pore system. One has to keep in mind that none of the pores was explicitly modeled, but the rock fabric with its different rock phases was modeled. Pore-size distribution, connectivity, and tortuosity, which will determine the petrophysical behavior of the rock, are the results of this modeling process. Petrophysical and fluid-flow properties can, in turn, directly be calculated on the model discretizations at any desired resolution using established numerical algorithms (Bakke and Øren 1997; Hilfer and Manwart, 2001; Øren and Bakke 2002; Bakke et al., 2007). Single-phase and multiphase flow properties simulated on the rock model have to be compared with the corresponding laboratory data to further investigate the influence of the individual pore classes and their combinations on flow properties and recovery.

CONCLUSIONS

In this study, a new approach for reservoir rock modeling of a multiscale porosity dolostone is presented. The pore-size distribution resulting from the rock modeling process is found to be representative for the pore system of the reservoir dolostone at all investigated scales. The main conclusions follow:

1. The resolution versus volume challenge involved in any rock modeling and x-ray tomographic imaging is approached by incorporating rock

fabric information from large-scale low-resolution x-ray tomographic images and high-resolution electron microscope images and combining them in the modeling process.

2. The resulting rock model reproduces the original rock sample in terms of porosity, mineralogy, pore/matrix/cement ratio, microporosity, and volume of different matrix phases, as well as dolomite crystal appearances and sizes.
3. A comparison of the pore sizes of the model and of the MCT control volumes showed that the pore systems could be captured using our modeling technique. Comparison in the range of microporosity was only limited by the limited resolution of the MCTs.
4. Pore-size analysis combined with percolation analysis on different discretizations of the model revealed pore-throat radii of 1.5 to 6 μm for the largest interconnected pore network. This indicates that the intercrystalline micropores and mesopores and the moldic pores present in the rock are only connected through mudstone microporosity, which reduces absolute permeability expectations to the single-digit millidarcy range.
5. To be used for petrophysical characterization, MCT images of reservoir rocks must resolve the pore network that carries the mean flow. The percolation tests performed on the individual pore classes have shown that in presence of pores over several orders of magnitude in size, detailed knowledge of the rock is necessary a priori to select one or multiple appropriate resolutions for MCT imaging.

REFERENCES CITED

- Adler, P. M., C. G. Jacquin, and J. A. Quiblier, 1990, Flow in simulated porous media: *International Journal of Multiphase Flow*, v. 16, no. 4, p. 691–712, doi:10.1016/0301-9322(90)90025-E.
- Aguilera, R., 2002, Incorporating capillary pressure, pore-throat aperture radii, height above free-water table, and Winland r_{35} values on Pickett plots: *AAPG Bulletin*, v. 86, no. 4, p. 605–624, doi:10.1306/61EEDB5C-173E-8645000102C1865D.
- Aguilera, R., 2004, Integration of geology, petrophysics, and reservoir engineering for characterization of carbonate reservoirs through Pickett plots: *AAPG Bulletin*, v. 88, no. 4, p. 433–446, doi:10.1306/12010303071.
- Bakke, S., and P. E. Øren, 1997, 3-D pore-scale modeling of sandstones and flow simulations in the pore networks: *Society of Petroleum Engineers Journal*, v. 2, no. 2, p. 136–149.
- Bakke, S., S. Roth, R. J. Held, and H. G. Rueslåtten, 2007, Pore-scale modeling of carbonate reservoir rocks: *International Symposium of the Society of Core Analysts*, Calgary, Canada, paper SCA2007-18, 12 p.
- Biswal, B., P.-E. Øren, R. J. Held, S. Bakke, and R. Hilfer, 2007, Stochastic multiscale model for carbonate rocks: *Physical Review E*, v. 75, no. 6, 5 p., doi:10.1103/PhysRevE.75.061303.
- Biswal, B., R. J. Held, V. Khanna, J. Wang, and R. Hilfer, 2009a, Toward precise prediction of transport properties from synthetic computer tomography of reconstructed porous media: *Physical Review E*, v. 80, no. 4, 13 p., doi:10.1103/PhysRevE.80.041301.
- Biswal, B., P.-E. Øren, R. J. Held, S. Bakke, and R. Hilfer, 2009b, Modeling of multiscale porous media: *Image Analysis and Stereology*, v. 28, p. 23–34.
- Choquette, P. W., and L. C. Pray, 1970, Geologic nomenclature and classification of porosity in sedimentary carbonates: *AAPG Bulletin*, v. 54, no. 2, p. 207–244.
- Dunham, R. J., 1962, Classification of carbonate rocks according to their depositional texture, *in* W. E. Ham, ed., *Classification of carbonate rocks: A symposium: AAPG Memoir 1*, p. 108–121.
- Embry, A. F., and J. E. Klován, 1971, A Late Devonian reef tract on northeastern Banks Island, N.W.T.: *Bulletin of Canadian Petroleum Geology*, v. 19, no. 4, p. 730–781.
- Folk, R. L., 1959, Practical petrographic classification of limestones: *AAPG Bulletin*, v. 43, no. 1, p. 1–38.
- Folk, R. L., 1962, Spectral subdivision of limestone types, *in* W. E. Ham, ed., *Classification of carbonate rocks: A symposium: AAPG Memoir 1*, p. 62–84.
- Ghous, A., et al., 2008, 3-D imaging of reservoir core at multiple scales: Correlations to petrophysical properties and pore-scale fluid distributions: *International Petroleum Technology Conference*, Kuala Lumpur, Malaysia, December 3–5, 10 p., doi:10.2523/12767-MS.
- Hazlett, R. D., 1997, Statistical characterization and stochastic modeling of pore networks in relation to fluid flow: *Mathematical Geology*, v. 29, no. 6, p. 801–822, doi:10.1007/BF02768903.
- Hilfer, R., 2000, Local porosity theory and stochastic reconstruction for porous media, *in* K. R. Mecke and D. Stoyan, eds., *Statistical physics and spatial statistics: Lecture notes in physics*: Berlin, Germany, Springer, v. 554, p. 203–241.
- Hilfer, R., and C. Manwart, 2001, Permeability and conductivity for reconstruction models of porous media: *Physical Review E*, v. 64, no. 2, 4 p., doi:10.1103/PhysRevE.64.021304.
- Hoshen, J., and R. Kopelman, 1976, Percolation and cluster distribution: I. Cluster multiple labeling technique and critical concentration algorithm: *Physical Review B*, v. 14, no. 8, p. 3438–3445, doi:10.1103/PhysRevB.14.3438.
- Kerans, C., J. F. Lucia, and R. K. Senger, 1994, Integrated

- characterization of carbonate ramp reservoirs using Permian San Andres Formation outcrop analogs: *AAPG Bulletin*, v. 78, no. 2, p. 181–216.
- Latief, F., B. Biswal, U. Fauzi, and R. Hilfer, 2010, Continuum reconstruction of the pore scale microstructure for Fontainebleau Sandstone: *Physica A*, v. 389, p. 1607–1618.
- Lønøy, A., 2006, Making sense of carbonate pore systems: *AAPG Bulletin*, v. 90, no. 9, p. 1381–1405, doi:[10.1306/03130605104](https://doi.org/10.1306/03130605104).
- Lucia, F. J., 1983, Petrophysical parameters estimated from visual description of carbonate rocks: A field classification of carbonate pore space: *Journal of Petroleum Technology*, v. 35, p. 626–637.
- Lucia, F. J., 1995, Rock-fabric/petrophysical classification of carbonate pore space for reservoir characterization: *AAPG Bulletin*, v. 79, no. 9, p. 1275–1300.
- Lucia, F. J., 1999, Characterization of petrophysical flow units in carbonate reservoirs: Discussion: *AAPG Bulletin*, v. 83, no. 7, p. 1161–1163.
- Manwart, C., S. Torquato, and R. Hilfer, 2000, Stochastic reconstruction of sandstones: *Physical Review E*, v. 62, no. 1, p. 893–899, doi:[10.1103/PhysRevE.62.893](https://doi.org/10.1103/PhysRevE.62.893).
- Martin, A. J., S. T. Solomon, and D. J. Hartmann, 1997, Characterization of petrophysical flow units in carbonate reservoirs: *AAPG Bulletin*, v. 81, no. 5, p. 734–759.
- Øren, P. E., and S. Bakke, 2002, Process-based reconstruction of sandstones and prediction of transport properties: *Transport in Porous Media*, v. 46, no. 2–3, p. 311–343, doi:[10.1023/A:1015031122338](https://doi.org/10.1023/A:1015031122338).
- Sahagian, D. L., and A. A. Proussevitch, 1998, 3-D particle size distributions from 2-D observations: Stereology for natural applications: *Journal of Volcanology and Geothermal Research*, v. 84, p. 173–196, doi:[10.1016/S0377-0273\(98\)00043-2](https://doi.org/10.1016/S0377-0273(98)00043-2).
- Silin, D., and T. Patzek, 2006, Pore space morphology analysis using maximal inscribed spheres: *Physica A*, v. 371, p. 336–360, doi:[10.1016/j.physa.2006.04.048](https://doi.org/10.1016/j.physa.2006.04.048).
- Wright, P. V., 1992, A revised classification of limestones: *Sedimentary Geology*, v. 76, p. 177–185, doi:[10.1016/0037-0738\(92\)90082-3](https://doi.org/10.1016/0037-0738(92)90082-3).
- Wu, K., A. Ryazanov, M. I. J. van Dijke, Z. Jiang, J. Ma, G. D. Couples, and K. S. Sorbie, 2008, Validation of methods for multiscale pore space reconstruction and their use in prediction of flow properties of carbonate: Proceedings of the International Symposium of the Society of Core Analysts, Abu Dhabi, U.A.E., paper SCA2008-34, 12 p.